

# The effect of detector sampling in wavefront-coded imaging systems

G Muyo and A R Harvey

School of Engineering and Physical Sciences, Heriot-Watt University,  
Edinburgh EH14 4AS, UK

E-mail: [a.r.harvey@hw.ac.uk](mailto:a.r.harvey@hw.ac.uk)

Received 9 October 2008, accepted for publication 4 December 2008

Published 18 March 2009

Online at [stacks.iop.org/JOptA/11/054002](http://stacks.iop.org/JOptA/11/054002)

## Abstract

We present a comprehensive study of the effect of detector sampling on wavefront-coded systems. Two important results are obtained: the spurious response ratios are reduced in wavefront-coded systems with a cubic phase mask and detector sampling does not compromise the restoration of wavefront-coded images with extended depth of field. Rigorous computer simulation of sampled wavefront-coded images shows an increased signal-to-aliased-noise ratio of up to 16% for a cubic phase mask with  $\alpha = 5\lambda$ .

**Keywords:** wavefront coding, detector sampling, aliasing, digital image processing

## 1. Introduction

There has been a recent growth of interest in the use of computational imaging techniques to provide improved performance or an extra degree of freedom in the design process [1]. One example of these hybrid optical/digital techniques is wavefront coding which employs a refractive phase mask, to produce a non-conventional point-spread function (PSF), combined with post-detection electronic processing to recover an image. The salient advantage is that a high-quality imaging can be achieved with greater tolerance to aberrations than is possible with traditional optical imaging [2].

In modern optical systems the optical image is sampled using a pixelated detector. Good optical sensitivity requires large pixels and fast optics, and so it is common that the coded image at the focal plane is undersampled by the pixelated detector [3–5], which introduces sampling artefacts due to aliasing. Subsequent to image recovery, the spatial frequency content of the image is mixed down into the baseband of the image where it interferes with the image spatial frequencies that fall within the baseband. This recorded image, with alias artefacts, is then modulated by the inverse filter used for image recovery. In this paper, for the first time to our knowledge, we appraise the significance of artefacts introduced into recovered images by aliasing in the recorded wavefront-coded images.

In section 2, using Fourier theory, we present a brief introduction to the response function of a sampled imaging system. The response function concept is similar to the optical

(OTF) function approach, although sampled imaging systems in which aliasing occurs are not shift invariant. Our analysis follows the work by Vollmerhausen *et al* [6] and Boreman [7], who provide a comprehensive aliasing model for conventional sampled systems using Fourier theory. In section 3, the same method is applied to a wavefront-coded imaging system with a cubic phase mask for coding strengths in the range  $0 \leq \alpha \leq 10\lambda$ , and the impact of sampling on the performance is investigated by means of simple metrics.

Finally, in section 4, we present simulations of the acquisition of sampled images with conventional and wavefront-coded imaging systems, based on the continuous/discrete/continuous imaging model derived by Park *et al* [8]. This characterizes aliasing as an additive scene-dependent noise and allows us to apply a signal-to-aliased-noise ratio metric to the sampled images and evaluate the effects that coding and decoding an image have on information content and aliasing artefacts.

## 2. Overview of the response function of a sampled imaging system

The response function describes the spatial frequency transfer function of a sampled imaging system and therefore provides information about the sampling artefacts that will be apparent in the image.

The response function of a sampled imaging system can be derived by characterizing the system response to a point

source. This is analogous to the method employed in non-sampled imaging systems; however, the response for the sampled system in the presence of aliasing is not *isoplanatic* or shift invariant: the system point-spread function and its Fourier transform vary with the relative positions of the point source to the sampling locations.

To simplify the mathematics, and without loss of generality, we restrict the study to a one-dimensional sampling process. For most practical sampled imaging systems, the complete image formation of the point source by an array of discrete detectors may be separated into two stages: the pre-sampling and sampling components. In the Fourier domain, the pre-sampling component accounts for the spatial frequency filtering due to the optics and finite size of the detectors, which are described by the OTF,  $H_{\text{opt}}$ , and the pixel or footprint transfer function,  $H_{\text{pix}}$ , respectively. The effect of spatial averaging over pixels of finite size is well known, and can be expressed as [7]

$$H_{\text{pix}}(\xi) = \text{sinc}(p\xi) = \frac{\sin(\pi p\xi)}{\pi p\xi} \quad (1)$$

where  $p$  is the full width of the pixel and  $\xi$  is the spatial frequency.

The sampling component of the response function can be represented by a comb of delta functions with sampling frequency  $f_{\text{sam}} = 1/X$ , where  $X$  is the interval between sampling points; thus

$$\perp\perp(\xi) = \sum_{n=-\infty}^{+\infty} \delta(\xi - nf_{\text{sam}}). \quad (2)$$

The three transfer functions  $H_{\text{opt}}$ ,  $H_{\text{pix}}$ , and  $\perp\perp$  multiply in the frequency domain to yield a combined response function for the imaging and sampling process, which yields [6]

$$R(\xi, \phi) = H_{\text{pix}}(\xi) \sum_{n=-\infty}^{+\infty} H_{\text{opt}}(\xi - nf_{\text{sam}}) \exp(in\phi). \quad (3)$$

It can be observed from (3) that the sampling process replicates the OTF,  $H_{\text{opt}}$ , at each integer  $n$  multiple of the sampling frequency  $f_{\text{sam}} = 1/X$ . All of the replicated spectra are multiplied by the pixel transfer function  $H_{\text{pix}}$  centred at the spatial frequency origin  $\xi = 0$  to yield the final spectrum. Each replicated spectrum varies in phase from the adjacent spectrum by the sample phase increment,  $\phi$ . Due to this phase variation, the sum in (3) is a function of  $\phi$ , and therefore the sampled response function  $R(\xi, \phi)$  will depend on the relative position of the pre-sampled point-spread function and the sampling points. The mathematical derivation of the sampling process shows two distinct contributions to  $R(\xi, \phi)$ : a transfer function and a *spurious response* component. The transfer function or *baseband spectrum* corresponds to  $n = 0$  and is independent of the sampling interval; it is simply the product of the OTF  $H_{\text{opt}}$  and the transfer function of the pixel  $H_{\text{pix}}$ . The spurious response is determined by multiplying  $H_{\text{pix}}$  by all the replicated spectra except the one located at the origin ( $n = 0$ ), and is conditioned by the sampling frequency  $f_{\text{sam}}$  and sampling phase  $\phi$ . The phase dependence of the spurious response

accounts for variations in the system PSF as the detector array is moved across the point source. The region of overlap between the spurious response and the baseband spectrum varies with the sampling frequency and is the main indicator of the magnitude of the sampling artefact in the image. For small sampling frequencies, the spurious response completely corrupts the baseband.

### 3. Response function of a sampled imaging system with wavefront coding

As an illustrative example, we consider an imaging system with a cubic phase mask in the aperture stop and quantify the impact of sampling on the overall OTF performance, and in particular, the effect of aliasing on the restorability of wavefront-coded images with extended depth of field. In this assessment, no post-detection display transfer functions such as the MTFs from the observer's eye and display (cathode ray tube spot, LCD, etc) are included. The same sampling model is applied to the imaging system without the cubic phase mask and the results obtained from both schemes before and after post-detection digital signal processing are compared.

The imaging system consists of an optical system with cut-off frequency  $f_{\text{cut}}$  ( $f_{\text{cut}} = 1/\lambda F/\#$ , where  $\lambda$  is the wavelength and  $F/\#$  is the  $f$ -number of the lens) and a focal plane array with pixel pitch  $X$  such that the sampling frequency is half the optical cut-off frequency; thus  $f_{\text{sam}} = f_{\text{cut}}/2$ . The Nyquist frequency,  $f_{\text{nyq}}$ , of this imaging system is then  $f_{\text{nyq}} = f_{\text{sam}}/2 = f_{\text{cut}}/4$ . We assume a pixel fill-factor of 100%. This generic imaging system is comparable to an uncooled thermal imager with an  $F/1.2$  germanium optics ( $f_{\text{cut}} = 80 \text{ cyc mm}^{-1}$  at wavelength  $\lambda = 10.5 \mu\text{m}$ ) and focal plane array with pixel size  $X = 25 \mu\text{m}$  (Nyquist frequency  $f_{\text{nyq}} = 20 \text{ cycles mm}^{-1}$ , assuming a 100% fill-factor). In the visible region, for example, this sampled imaging system represents an  $F/5.6$  optical system at  $\lambda = 0.587 \mu\text{m}$  together with a focal plane array whose pixel pitch is  $6.45 \mu\text{m}$ .

The optical modulation transfer function (MTF), replicated spectra, and pixel MTF of the sampled imaging system with and without a cubic phase mask are shown in figure 1 for  $\alpha = 5\lambda$ . In this system, only the replicas with  $-2 \leq n \leq +2$  in equation (3) contribute sampling artefacts, and replicas centred on  $n > 2$  are strongly attenuated by the pixel transfer function as this becomes increasingly small at high frequencies. Due to the sub-Nyquist sampling of the detector the replicas are very close together and overlap severely, causing significant corruption of the information in the baseband. Furthermore, replicas  $\exp(-i2\phi)$  and  $\exp(-i\phi)$  in the negative frequency axis spread over the positive axis and vice versa. Note that only the magnitudes are displayed in figure 1 but the phase must also be included when calculating the spurious response. A factor in the wavefront-coded system is that the antisymmetry of the cubic phase mask function produces a complex OTF which adds an extra frequency-dependent phase factor to the replicated spectra [9]. Consequently, the amplitude of the entire response function  $R$  at any one frequency is the complex summation of all terms, and the result will depend not only on sample phase  $\phi$  but also on

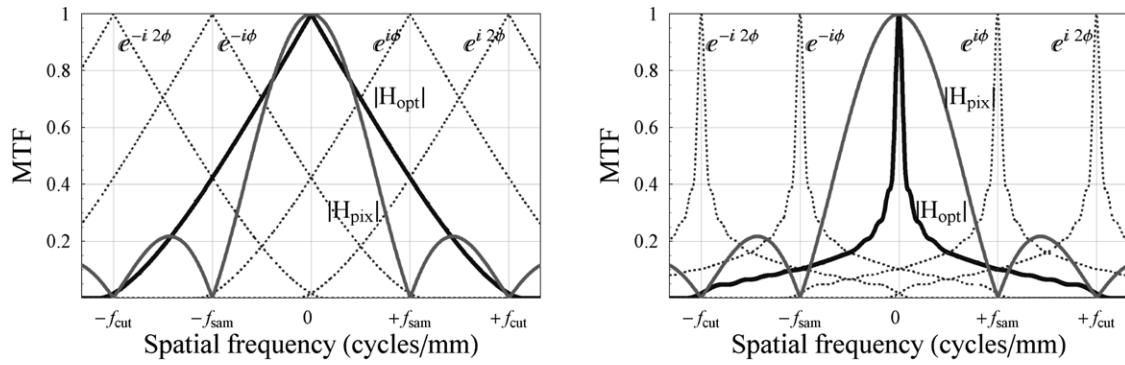


**Figure 1.** Optics MTF (solid black curve), replicated spectra (dotted) and pixel transfer function (solid grey curve) of a sampled imaging system without (left) and with a cubic phase mask  $\alpha = 5\lambda$  prior to post-detection processing (right).

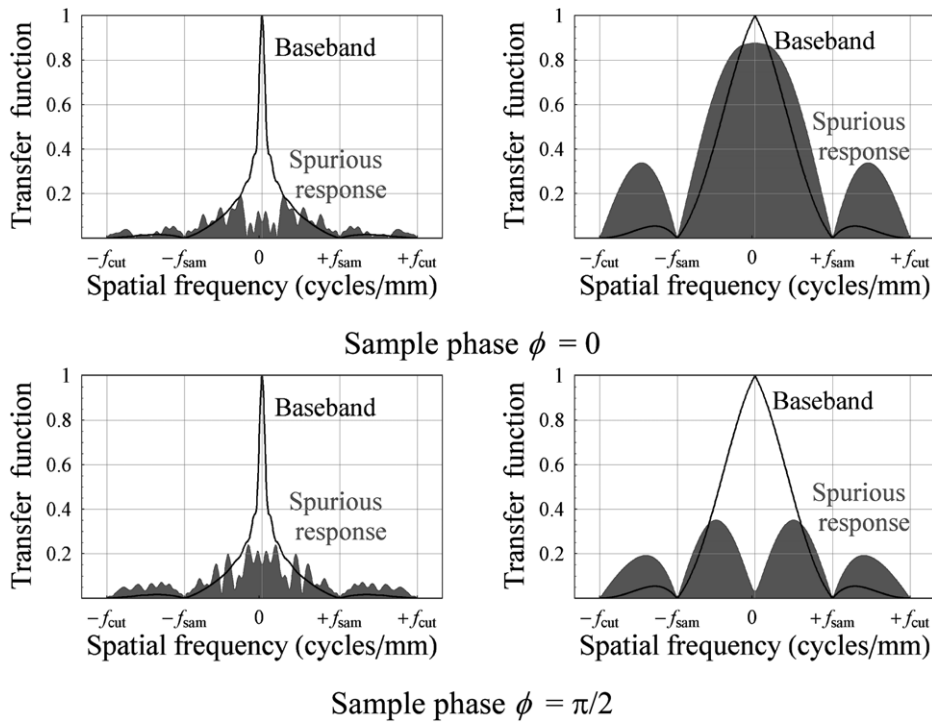


**Figure 2.** Magnitude of the transfer function (optics OTF and pixel OTF) and spurious response (replicated spectra and pixel OTF centred at the frequency origin) as a function of phase sampling for a wavefront coding system with a cubic phase mask  $\alpha = 5\lambda$  (left) and a traditional system (right) for two values of the sample phase. No post-detection digital processing has been applied.

the magnitude of the wavefront-coded distortion. As a result, the complex summation of wavefront-coded OTFs produces a highly modulated and intricate spurious response across the spatial frequency domain, as illustrated in figure 2 for  $\phi = 0$  and  $\pi/2$ . The baseband and spurious response in figure 2 were calculated from (3), i.e.

$$\text{Baseband: } B(\xi) = H_{\text{pix}}(\xi)H_{\text{opt}}(\xi)$$

$$\begin{aligned} \text{Spurious response: } S(\xi, \phi) = & H_{\text{pix}}(\xi) \\ & \times \sum_{n=-2}^{+2} H_{\text{opt}}(\xi - nf) \exp(in\phi) \quad \text{with } n \neq 0. \end{aligned} \quad (4)$$

Note that the wavefront-coded baseband and spurious terms displayed in figure 2 correspond to the sampled PSF at the sensor and not to the decoded PSF: post-detection

image processing must be applied in order to draw a valid comparison with the traditional sampled imager. However, some performance characteristics can be explained from analysing these response curves. At high spatial frequencies, greater than the Nyquist frequency, the spurious response produces sharp edges and blocky pixels in the image. This can be clearly observed in the sampled image of a spoke target, shown in figure 3, where the high-frequency content of the spurious response of the traditional system is very large, meaning that the sharp pixel edges become much more visible than in the wavefront-coded image prior to restoration. In the latter, the aggregate of the cubic phase mask OTF and pixel transfer function lowers the baseband and the spurious response, attenuating the high-frequency content and adding further blur to the image. When signal processing is applied

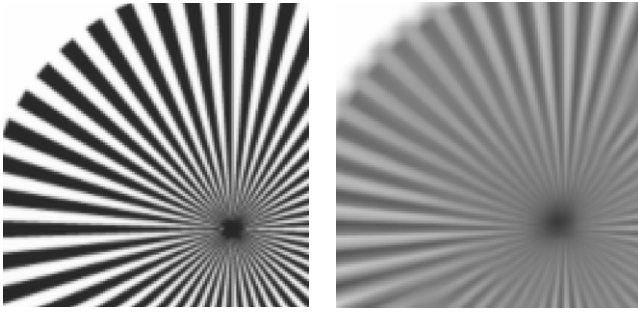


**Figure 3.** Detected image with a conventional sampled traditional optical system (left) and with a sampled wavefront-coded system (right). Clearly, the significantly higher spurious response content of the traditional system compared to the wavefront-coded system accentuates the blocky nature of the pixels.

to the sampled-coded image to compensate for the effects of the cubic mask, the filtering restores simultaneously the wavefront-coded bandpass and the spurious response; hence, aliasing-related artefacts become more apparent in the restored image. The absence of zeros in the baseband spectrum with the cubic phase mask allows the use of a simple inverse filter to recover a transfer function identical to that of the traditional system. The inverse filter is implemented by using the following expressions:

$$\text{Restored baseband: } B'(\xi) = \frac{H_{\text{dif}}(\xi)}{H_{\text{opt}}(\xi)} B(\xi)$$

$$\text{Restored spurious response: } S'(\xi, \phi) = \frac{H_{\text{dif}}(\xi)}{H_{\text{opt}}(\xi)} S(\xi, \phi) \quad (5)$$

where  $H_{\text{dif}}/H_{\text{opt}}$  is centred at the spatial frequency origin  $\xi = 0$  and applied only for  $-f_{\text{cut}} \leq \xi \leq f_{\text{cut}}$ . With the aim of providing a clear analysis of aliasing effects, no noise is considered in the model; in this way we ensure that the basebands of the traditional and wavefront-coded systems are identical after restoration. The restored baseband and spurious response of the wavefront-coded system are shown in figure 4 for sampling phases  $\phi = 0$  and  $\pi/2$ . Although the baseband response of the wavefront-coded system is identical to that of the traditional system, comparison with figure 2 shows that the magnitude of the additional restored spurious response is significantly reduced, particularly in the low-spatial-frequency region. This effect arises from the

highly variable phase introduced by the cubic phase mask across the spatial frequency spectrum. Furthermore, any other antisymmetric phase mask, such as the generalized cubic phase mask [10], will produce similar effects: it is the rapid phase changes from adjacent spatial frequencies so characteristic of an antisymmetric mask that produce highly oscillatory and relatively low spurious responses. One final aspect worth remarking is that the inverse filter also modifies the phase of the net spurious response at any given spatial frequency, and therefore aliasing artefacts may appear only in certain features of the restored image, whilst not being evident in an equivalent traditional sampled image.

### 3.1. Calculation of the spurious response ratio with a cubic phase mask

The impact of sampling on the performance of a sampled imaging system can be evaluated by calculating the spurious response ratio. This metric characterizes the effect of the spurious response in the detected image using only a single quantity. Three different spurious response ratios have been used in this paper, derived from similar definitions in [11]: the total integrated spurious response ratio (SRR), the in-band spurious response ratio (SRR<sub>ib</sub>), and the out-of-band spurious response ratio (SRR<sub>ob</sub>):

$$\text{SRR}(\phi) = \frac{\int_{-\infty}^{+\infty} |S'(\xi, \phi)| d\xi}{\int_{-\infty}^{+\infty} |B'(\xi)| d\xi} \quad (6)$$

$$\text{SRR}_{\text{ib}}(\phi) = \frac{\int_{-f_{\text{nyq}}}^{+f_{\text{nyq}}} |S'(\xi, \phi)| d\xi}{\int_{-\infty}^{+\infty} |B'(\xi)| d\xi} \quad (7)$$

$$\text{SRR}_{\text{ob}}(\phi) = \text{SRR}(\phi) - \text{SRR}_{\text{ib}}(\phi). \quad (8)$$

The integral of the total spurious response magnitude normalized to the integrated baseband magnitude is taken as a measure of image artefact content in the imaging process. SRR<sub>ib</sub> takes into account the in-band aliasing, and it is defined as the area underlying the part of the spurious response falling inside the Nyquist frequency range normalized by the integral of the entire baseband response. The total and in-band spurious response ratios were calculated for the traditional and restored wavefront-coded systems as a function of the sample phase  $\phi$ . As shown in figure 5, depending on the phase and frequency content of the replicated spurious responses, their net effect

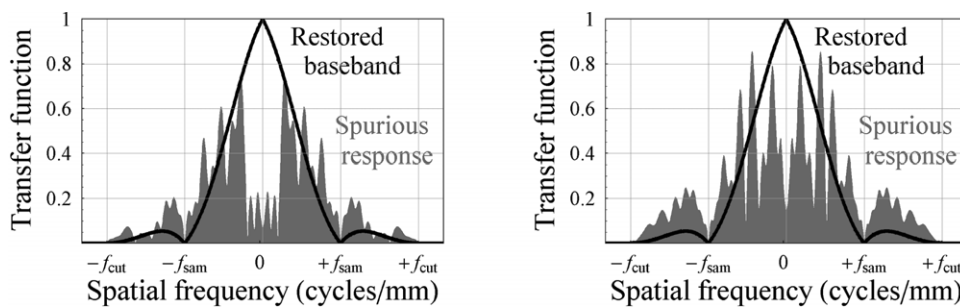


**Figure 4.** Magnitude of the baseband and the spurious response for the wavefront-coded system with a cubic phase mask  $\alpha = 5\lambda$  after inverse filtering with sampling phase  $\phi = 0$  (left) and  $\phi = \pi/2$  (right).

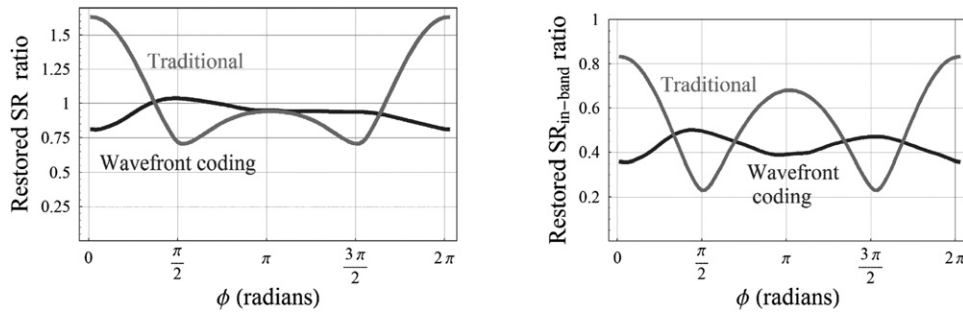


**Figure 5.** Magnitude of the total spurious response (left) and magnitude of the in-band spurious response (right), as a function of phase sampling for both traditional (grey curve) and restored wavefront coding systems (dark curve).

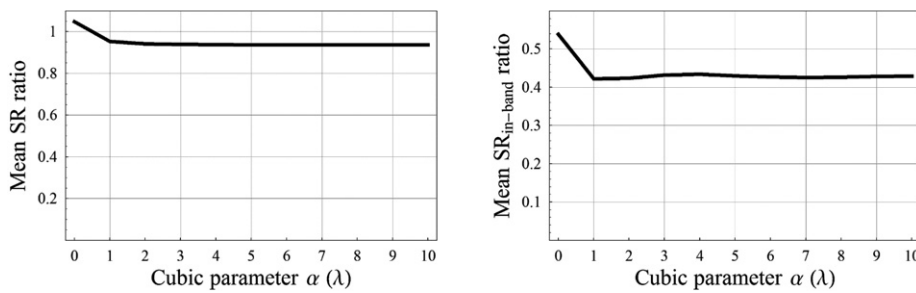


**Figure 6.** Mean magnitude over the sampling phase of the full-band (left) and in-band (right) spurious response ratios, as a function of the cubic phase mask parameter  $\alpha$ .

becomes destructive or constructive in nature and oscillates in magnitude. However, the SRR can be condensed into a single number in order to predict a good performance measurement by taking the average across the sampling phase  $0 \leq \phi \leq 2\pi$ . The phase-averaged SRR and  $SRR_{ib}$  were calculated for the above-mentioned conventional sampled imager:  $SRR = 1.05$  and  $SRR_{ib} = 0.54$ ; and for the wavefront-coded sampled imager after restoration:  $SRR = 0.94$  and  $SRR_{ib} = 0.43$ . The calculation of phase-averaged spurious response ratios was also extended to cubic phase masks with coding strengths  $0 \leq \alpha \leq 10\lambda$ . The results are illustrated in figure 6 and show that the total and in-band spurious responses ratios remain practically constant with  $\alpha$ . This suggests that beyond a certain degree of mask-induced phase change between adjacent spatial frequencies, the number of destructive and constructive spurious events balances out, and hence the spurious response ratios remain unchanged for any value of  $\alpha > 1\lambda$ .

### 3.2. Defocus tolerance with a wavefront-coded sampled imaging system

We have shown that detector sampling of wavefront PSFs does not affect in a negative way the restoration process by which the diffraction-limited performance of the baseband spectrum is subsequently recovered. Furthermore, we have demonstrated that, in the absence of noise, wavefront coding enables a slight reduction of artefacts in the restored images as expressed by the spurious response ratio. In this section, the impact of sampling on the ability of a wavefront-coded system to mitigate defocus aberration is investigated. Whereas for a conventional imaging system defocus causes a marked reduction or even nulls in the

MTF, for a wavefront-coded system, variations in magnitude are much less, but variations in the phase of the OTF can introduce artefacts. We consider here how these artefacts are affected by aliasing. We restrict the discussion to an example cubic phase mask with  $\alpha = 5\lambda$ , although the results shown here can be extended to any antisymmetric phase mask, and in particular to the family of cubic phase masks with different values of  $\alpha$ .

The pre-processed (detected) baseband  $B(\xi)$  and spurious response  $S(\xi, \phi)$  of a wavefront-coded system were generated for a set of defocus coefficients  $W_{20}$  varying from 0 to 5 in units of wavelength. Subsequently, the coded basebands and spurious response functions were inverse filtered using the wavefront-coded OTF associated with no defocus and the diffraction-limited OTF. This process can be expressed mathematically by simply introducing the defocus variable  $W_{20}$  in (5), which yields

$$\begin{aligned} \text{Restored baseband: } B'(\xi, W_{20}) &= \frac{H_{\text{dif}}(\xi)}{H_{\text{opt}}(\xi, W_{20} = 0)} B(\xi, W_{20}) \end{aligned} \tag{9}$$

$$\begin{aligned} \text{Restored spurious response: } S'(\xi, \phi, W_{20}) &= \frac{H_{\text{dif}}(\xi)}{H_{\text{opt}}(\xi, W_{20} = 0)} S(\xi, \phi, W_{20}). \end{aligned}$$

The result of restoring the baseband  $B(\xi, W_{20})$  with the in-focus OTF  $H_{\text{opt}}(\xi, 0)$  is identical to that of a well-sampled wavefront-coded imager where the baseband contains the pixel transfer function. The inverse filtering of the defocused basebands introduces identical phase and magnitude

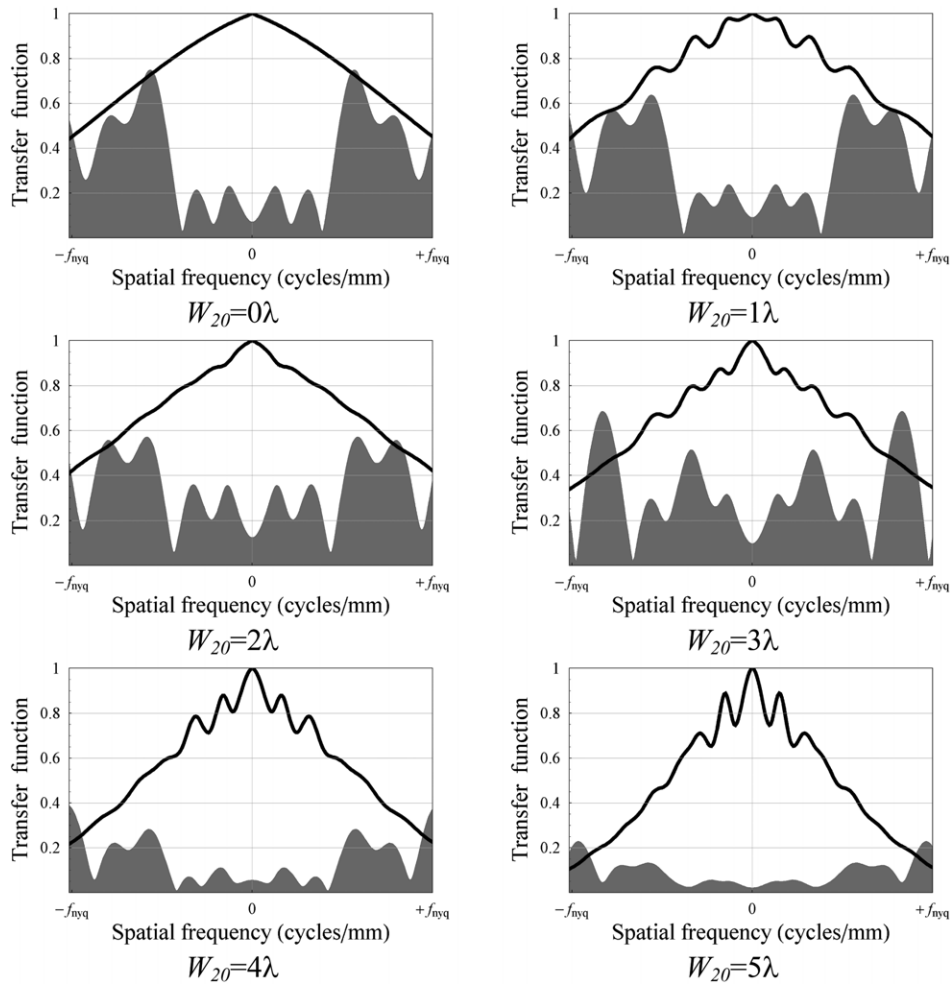


**Figure 7.** Magnitude of the baseband (dark plot) and spurious response (solid) for a wavefront-coded system with a cubic phase mask  $\alpha = 5\lambda$  after post-detection image processing for various amounts of defocus  $W_{20}$ . Magnitudes displayed up to the Nyquist frequency.

mismatches at exactly the same spatial frequencies as the well-sampled wavefront-coded system. Thus, detector sampling has no effect on the ability of wavefront coding to alleviate defocus aberration. This is illustrated in figure 7, where the restored basebands as a function of defocus are shown to exhibit the same characteristic magnitude modulations and high-frequency decline as the well-sampled MTFs [9]. Also shown in figure 7 is the inverse-filtered spurious response as a function of the defocus coefficient  $W_{20}$ . Clearly, the spurious response becomes progressively suppressed as increasing defocus degrades the medium and high spatial frequencies which are subsequently mirrored under the Nyquist band. This is an expected result for both the wavefront-coded and conventional sampled imagers, since aliasing artefacts are reduced in magnitude with defocus due to the suppression of the medium and high spatial frequencies.

The variation of the sampling-phase-averaged total and in-band spurious response ratio with defocus is depicted in figure 8. Interestingly, these figures depict implicitly the value of defocus of  $3\lambda$  above which the aberration becomes dominant and the aliasing ratio starts to decrease; as a result, the restored wavefront-coded response function is no longer invariant to defocus.

The results presented in this section take into account only the sampled transfer function to characterize the sampled imaging system, whereas the sampling artefacts produced by an imaging system also depend on the actual scene being imaged; we shall conclude the study in the last section with a numerical evaluation of the sampling effects that arise in sampled images of two standard scenes.

#### 4. Simulation and aliasing evaluation of sampled images

To complete our study on sampling and its effect on wavefront-coded imaging systems, we make use of a comprehensive imaging model to simulate sampled images that properly accounts for the low-pass filtering of the optics, the blurring and sampling of the detector array, and the amplification of higher spatial frequencies in the digital processing. The imaging model employed is based on the model<sup>1</sup> described

<sup>1</sup> We do not include the image reconstruction stage as we are interested only in evaluating the effect of sampling at the output of the detector array of the traditional and wavefront-coded imaging system. Any image reconstruction step would be applied equally to both systems, and therefore no performance differences would be introduced during this process.

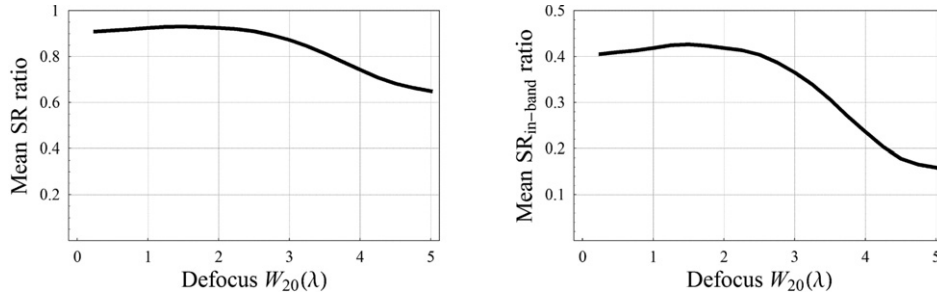


**Figure 8.** Mean magnitude across the sample phase of the full-band (left) and in-band (right) spurious response ratios, as a function of the defocus coefficient  $W_{20}$ , for  $\alpha = 5\lambda$  after post-detection image processing.

in detail by Park *et al* [8] which considers aliasing as a scene-dependent additive noise. It enables the baseband and spurious components of the sampled images to be calculated and displayed separately whilst providing metrics to quantify the magnitude of aliasing. The input to the simulation is a continuous scene  $o$  projected by the imaging optics onto the detector. The scene is low-pass filtered by the OTF, averaged by the pixel area, and sampled by a detector array to produce an  $N \times N$  digital image (for simplicity the detector is assumed to be square). In the case of the wavefront-coded system, the  $N \times N$  image is subsequently decoded to obtain a sharp image. For clarity, we assume that no random noise is introduced by the sensor electronics. The continuous scene  $o$  is assumed to be bandlimited and is represented by a Fourier series whose coefficients are given by  $O[v_1, v_2]$ . The Fourier coefficients can be obtained from an  $M \times M$  high-resolution digital image of the scene. To model a sampled imaging system properly  $M$  must be chosen several times larger than  $N$  so as to allow for significant spectral energy beyond the sampling frequency.

By considering aliasing as scene-dependent additive noise, we can express the discrete Fourier spectrum of a sampled image as the sum of two components (in an analogous way to the response function of a sampled imager); thus

$$I[v_1, v_2] = B_i[v_1, v_2] + S_i[v_1, v_2] \quad (10)$$

where  $B_i$  is the image baseband and the  $S_i$  is its aliased noise term or spurious response. The baseband (or Fourier spectrum of the pre-sampled image) is defined by

$$B_i[v_1, v_2] = H_{\text{pix}}(v_1/P, v_2/P) H_{\text{opt}}(v_1/P, v_2/P) O[v_1, v_2], \quad (11)$$

where  $P$  is the width of the square detector; thus  $P = NX$  ( $X$  the pixel pitch). The spurious components of the sampled image are calculated by adding replicas of the spectrum of the pre-sampled image (without including the pixel transfer function) shifted at multiples of the sampling frequency, which yields

$$\begin{aligned} S_i[v_1, v_2] &= H_{\text{pix}}(v_1/P, v_2/P) \\ &\times \sum_{k_1=-\infty}^{+\infty} \sum_{k_2=-\infty}^{+\infty} H_{\text{opt}}\left(\frac{v_1 - k_1 N}{P}, \frac{v_2 - k_2 N}{P}\right) \\ &\times O[v_1 - k_1 N, v_2 - k_2 N], \quad \text{with } [k_1, k_2] \neq [0, 0]. \end{aligned} \quad (12)$$

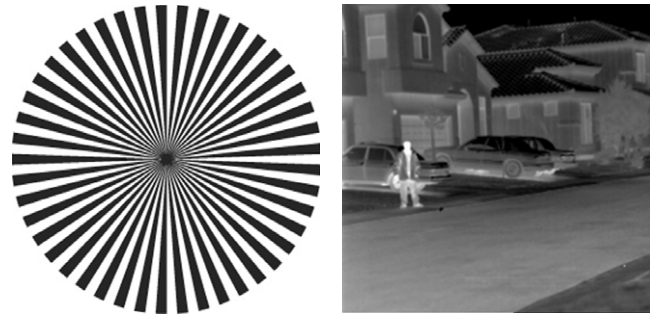


**Figure 9.** 1280  $\times$  1280 pixel high-resolution spoke target and thermal image for the sampling model. The original thermal image is from Sierra Pacific Innovations Corporation ([www.x20.org](http://www.x20.org)).

The functions with  $()$  and  $[\ ]$  are used to represent continuous and discrete components, respectively. Post-detection digital processing restores the wavefront-coded baseband spectrum to match the baseband spectrum of the traditional system, which we assume to be diffraction limited. Therefore, after restoration using an inverse filter, equations (11) and (12) become

$$B'_i[v_1, v_2] = \frac{H_{\text{dif}}(v_1/P_1, v_2/P_2)}{H_{\text{opt}}(v_1/P_1, v_2/P_2)} B_i[v_1, v_2], \quad (13)$$

and

$$S'_i[v_1, v_2] = \frac{H_{\text{dif}}(v_1/P_1, v_2/P_2)}{H_{\text{opt}}(v_1/P_1, v_2/P_2)} S_i[v_1, v_2]. \quad (14)$$

Aliasing can be quantified by comparing both components referenced to the input scene:  $R_b = B'_i[v_1, v_2]/O[v_1, v_2]$  and  $R_s = S'_i[v_1, v_2]/O[v_1, v_2]$ , provided  $O[v_1, v_2] \neq 0$ . The magnitude of these ratios allows us to establish the spatial frequency region where  $R_s > R_b$  and quantify the degree of the aliasing component.

This quantitative assessment has been applied to two high-resolution scenes, see figure 9: a spoke target and thermal image with 1280  $\times$  1280 pixels, sampled by a 320  $\times$  320 detector with sampling frequency at half the cut-off frequency of the optical system,  $f_{\text{sam}} = f_{\text{cut}}/2$  (equivalent to the imaging system used to derived the response function in section 3). The former scene enables ready observation of artefacts, whilst the latter enables a more representative appreciation of their subjective significance.

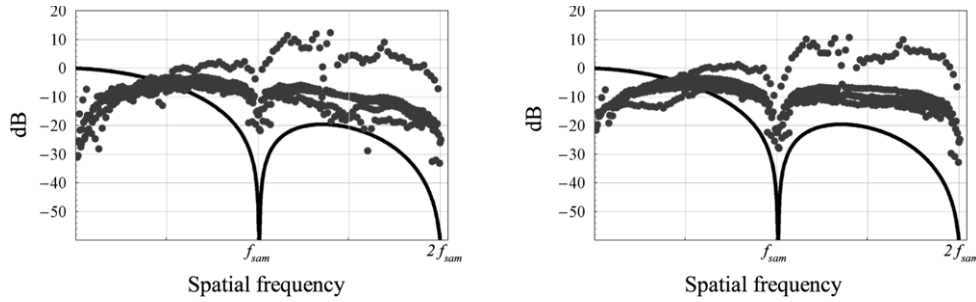


**Figure 10.** Magnitude of the baseband spectrum ratio  $B'_i/O$  (solid) and aliasing component ratio  $S'_i/O$  (dotted) of the spoke target imaged by the wavefront-coded system after restoration (left) and a traditional system (right).

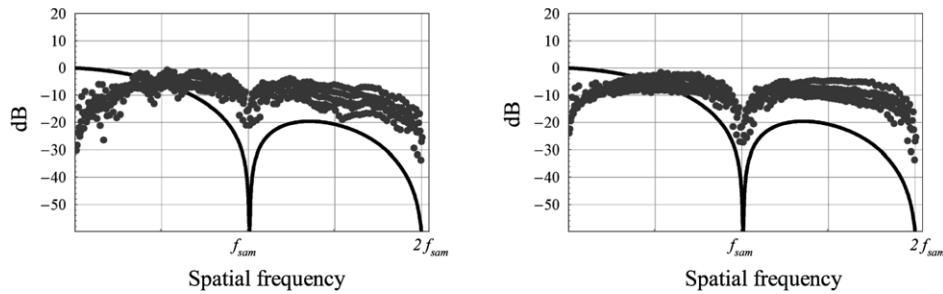


**Figure 11.** Magnitude of the baseband spectrum ratio  $B'_i/O$  (solid) and aliasing component ratio  $S'_i/O$  (dotted) of the thermal scene imaged by the wavefront-coded system after restoration (left) and a traditional system (right).

**Table 1.** Signal-to-aliased-noise ratio (SANR) of two scenes being imaged by a traditional and a wavefront-coded system after restoration.

Scenes	Traditional SANR	Restored wavefront-coded SANR
Spoke target	28	32
Thermal image	42	50

The absolute values of the ratios  $R_b$  and  $R_s$  along the spatial frequency axis  $[\nu_1, 0]$  are shown in figures 10 and 11 for the sampled images of the spoke target and thermal scene, respectively. The left column in the figures corresponds to the restored wavefront-coded system, and the right column to the traditional system. The solid dark curve represents  $|R_b[\nu_1, 0]|$  whilst the grey dots map  $|R_s[\nu_1, 0]|$ , both in decibels. Note that both ratios become zero at multiples of the sampling frequency of the detector where the nulls of the pixel transfer function occur. In good agreement with the results presented in the previous section, the baseband is dominant at low spatial frequencies up to approximately the Nyquist frequency, whereas the aliased ratio dominates at greater spatial frequencies. Due to the coarse sampling of the detector, the aliased component of the output image is significant. A closer investigation shows two important features consistent with our previous results: (1) the mean of the aliased component, given by  $S'_i[0, 0]$ , is smaller in the restored wavefront-coded images than in the traditional images; (2) the aliased components of the restored wavefront-coded images appear much more fluctuating as a result of the

increased number of interferometric modulations that occur in the spurious response.

To quantify the magnitude of aliasing with a single number we make use of the signal-to-aliased-noise ratio (SANR) defined by Park *et al* [8]. The ratio is given by the variance of the baseband over the variance of the aliased component:  $SANR = \sigma_b/\sigma_s$ , where

$$\sigma_b^2 = \sum_{\nu_1 \neq 0} \sum_{\nu_2 \neq 0} |B'_i[\nu_1, \nu_2]|^2 \quad \text{and} \quad (15)$$

$$\sigma_s^2 = \sum_{\nu_1 \neq 0} \sum_{\nu_2 \neq 0} |S'_i[\nu_1, \nu_2]|^2.$$

The SANR metric was applied to both restored wavefront-coded and traditional images, and the results are displayed in table 1. Note that the wavefront-coded images show a reduction in SANR of the order of 15% when compared to the traditional images, as predicted when we derived the transfer function of a sampled wavefront-coded imager. It is interesting to note that prior to restoration the wavefront-coded images presented an  $SANR = 170$  due to the defocus-invariant blur introduced by the phase mask. The assessment of the impact of aliasing on the recovery of the coded scene data must also be based on visual inspection of the restored images. Figure 12 illustrates the output images of the spoke and thermal scene respectively for both imaging systems. Clearly, post-detection digital processing restored the wavefront-coded images to an equivalent quality to that of a conventional imager in spite of all the intricate sampling interferences that occur and corrupt the baseband content: no significant difference can be observed between the decoded and conventional images.

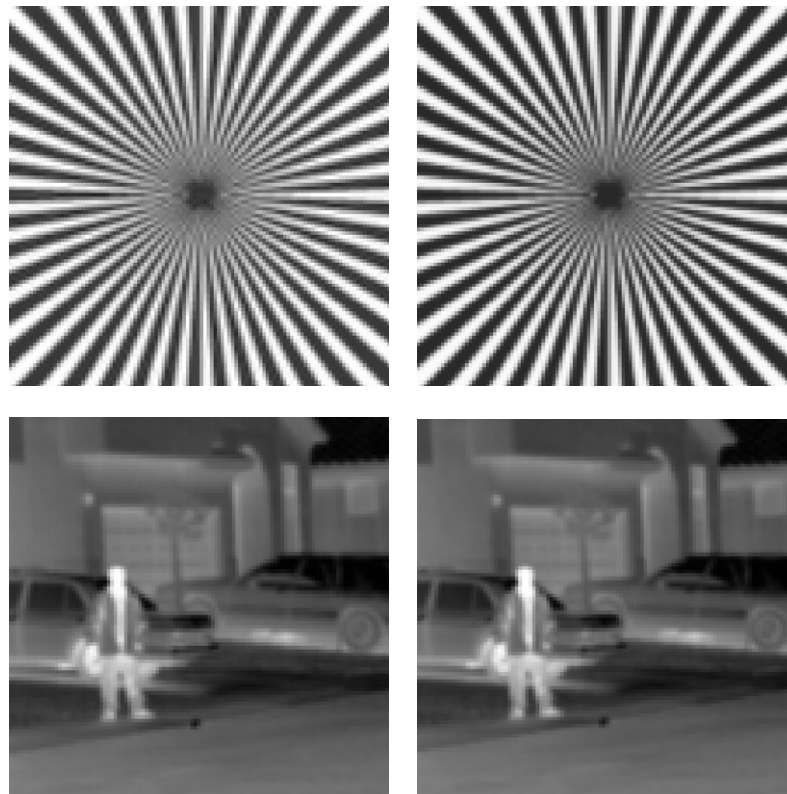


**Figure 12.** Details of the final output images for the wavefront-coded system (left) and traditional system (right). The original thermal image is from Sierra Pacific Innovations Corporation ([www.x20.org](http://www.x20.org)).

## 5. Conclusions

We have reported a comprehensive and rigorous assessment of the effect of detector sampling on wavefront-coded imaging systems that make use of cubic phase masks. The results showed for specific but representative systems with cubic phase mask parameter  $\alpha > 1\lambda$  a modest decrease in the full-band and in-band spurious response ratios (averaged across the sampling phase). The reduction in the spurious response ratios appears to be attributable to averaging of high-frequency interference between aliased components. Interestingly, this also suggests that wavefront coding can be employed as an anti-aliasing filter by means of introducing highly oscillatory phase gradients as opposed to other approaches whereby it is the magnitude of the spatial frequencies that is modified or suppressed, for example by defocusing the optical system.

Computer simulation of sampled imaging of standard scenes has also shown a reduced presence of sampling artefacts in terms of the signal-to-aliased-noise ratio for a wavefront-coded system with  $\alpha = 5\lambda$ . These results are consistent with those obtained in terms of the spurious response ratio. More importantly, we have also demonstrated that detector sampling does not prevent decoding the detector image to diffraction-limited (sampled) quality.

## Acknowledgment

This study was carried out with funding from QinetiQ Ltd, Malvern, UK.

## References

- [1] Mait J N, Athale R and van der Gracht J 2003 Evolutionary paths in imaging and recent trends *Opt. Express* **11** 2093–101
- [2] Dowski E R and Cathey W T 1995 Extended depth of field through wavefront coding *Appl. Opt.* **34** 1859–66
- [3] Muyo G, Singh A, Andersson M, Huckridge D and Harvey A 2006 Optimized thermal imaging with a singlet and pupil plane encoding: experimental realization *Proc. SPIE—Int. Soc. Opt. Eng.* **6395** 63950M
- [4] Harvey A R *et al* 2008 Digital image processing as an integral component of optical design *Proc. SPIE—Int. Soc. Opt. Eng.* **7061** 706104
- [5] Harvey A, Muyo G, Demenikov M and Lucotte B 2008 The principles and roles of hybrid optical/digital codecs in imaging *Proc. SPIE—Int. Soc. Opt. Eng.* **7113** 71130D
- [6] Vollmerhausen R and Driggers R 2000 *Analysis of Sampled Imaging Systems* (Bellingham, WA: SPIE Optical Engineering Press)
- [7] Boreman G D 2001 *Modulation Transfer Function in Optical and Electrooptical Systems* (Bellingham, WA: SPIE Optical Engineering Press)
- [8] Park S K and Rahman Z 1999 Fidelity analysis of sampled imaging systems *Opt. Eng.* **38** 786–800
- [9] Muyo G and Harvey A R 2005 Decomposition of the optical transfer function: wavefront coding systems *Opt. Lett.* **30** 2715–7
- [10] Prasad S, Torgersen T C, Pauca V P, Plemmons R J and van der Gracht J 2003 Engineering the pupil phase to improve image quality *Proc. SPIE—Int. Soc. Opt. Eng.* **5108** 1–12
- [11] Driggers R G, Vollmerhausen R and O’Kane B 1999 Equivalent blur as a function of spurious response of a sampled imaging system: application to character recognition *J. Opt. Soc. Am. A* **16** 1026–33